Evidence for distributed gas sources of hydrogen halides in the coma of comet 67P/Churyumov-Gerasimenko

Johan De Keyser[1,2⋆], Frederik Dhooghe[1], Kathrin Altwegg[3,4], Hans Balsiger[3], Jean-Jacques Berthelier[5], Christelle Briois[6], Ursina Calmonte[3], Gaël Cessateur[1], Michael R. Combi[7], Eddy Equeter[1], Björn Fiethe[8], Stephen Fuselier[9,10], Sébastien Gasc[3], Andrew Gibbons[1,11], Tamas Gombosi[7], Herbert Gunell[1], Myrtha Hässig[3,9], Léna Le Roy[4], Romain Maggiolo[1], Urs Mall[12], Bernard Marty[13], Eddy Neefs[1], Henri Rème[14,15], Martin Rubin[3], Thierry Sémon[3], Chia-Yu Tzou[3], Peter Wurz[3,4]

[1] *Royal Belgian Institute for Space Aeronomy, BIRA-IASB, Ringlaan 3, B-1180 Brussels, Belgium*
[2] *Center for mathematical Plasma Astrophysics, KULeuven, Celestijnenlaan 200B, B-3001 Heverlee, Belgium*
[3] *Physikalisches Institut, University of Bern, Sidlerstr. 5, CH-3012 Bern, Switzerland*
[4] *Center for Space and Habitability, University of Bern, Sidlerstr. 5, CH-3012 Bern, Switzerland*
[5] *LATMOS/IPSL-CNRS-UPMC-UVSQ, 4 Avenue de Neptune F-94100, Saint-Maur, France*
[6] *Laboratoire de Physique et Chimie de l'Environnement et de l'Espace (LPC2E), UMR CNRS 7328, Université d'Orléans, France*
[7] *Department of Climate and Space Sciences and Engineering, University of Michigan, 2455 Hayward, Ann Arbor, MI 48109, USA*
[8] *Institute of Computer and Network Engineering (IDA), TU Braunschweig, Hans-Sommer-Straße 66, D-38106 Braunschweig, Germany*
[9] *Space Science Directorate, Southwest Research Institute, 6220 Culebra Rd., San Antonio, TX 78228, USA*
[10] *University of Texas at San Antonio, San Antonio, TX, 78228, USA*
[11] *Service de Chimie Quantique et Photophysique, Université Libre de Bruxelles, 50 Avenue F. Roosevelt, B-1050 Brussels, Belgium*
[12] *Max-Planck-Institut für Sonnensystemforschung, Justus-von-Liebig-Weg 3, 37077 Göttingen, Germany*
[13] *Centre de Rech. Pétrographiques & Géochimiques, CRPG-CNRS, Univ. Lorraine, 15 rue N. D. des Pauvres, BP 20, 54501 Vandoeuvre lès Nancy, France*
[14] *Université de Toulouse; UPS-OMP; IRAP, Toulouse, France*
[15] *Institut de Recherches en Astrophysique et Planétologie, CNRS-IRAP; 9 Avenue du Colonel Roche, BP 44346, F-31028 Toulouse Cedex 4, France.*

Accepted XXX. Received YYY; in original form ZZZ

ABSTRACT

Rosetta has detected the presence of the hydrogen halides HF, HCl, and HBr in the coma of comet 67P/Churyumov-Gerasimenko. These species are known to freeze out on icy grains in molecular clouds. Analysis of the abundances of HF and HCl as a function of cometocentric distance suggests that these hydrogen halides are released both from the nucleus surface and off dust particles in the inner coma. We present three lines of evidence. First, the abundances of HF and HCl relative to the overall neutral gas in the coma appear to increase with distance, indicating that a net source must be present; since there is no hint at any possible parent species with sufficient abundances that could explain the observed levels of HF or HCl, dust particles are the likely origin. Second, the amplitude of the daily modulation of the halide-to-water density due to the rotation and geometry of 67P's nucleus and the corresponding surface illumination is observed to progressively diminish with distance and comet dust activity; this can be understood from the range of dust particle speeds well below the neutral gas expansion speed, which tends to smooth the coma density profiles. Third, strong halogen abundance changes detected locally in the coma cannot be easily explained from composition changes at the surface, while they can be understood from differences in local gas production from the dust particles.

Key words: comets:general – comets:individual:67P/Churyumov-Gerasimenko

⋆ E-mail: johan.dekeyser@aeronomie.be

1 INTRODUCTION

A comet is often considered to be a cold body made of ices and refractory material, which releases neutral gas by sublimation of the ices embedded among the refractory particles, thus leading to the formation of the neutral comet atmosphere or gas coma as well as a dust coma. Sublimation of mixtures of H_2O, CO, and/or CO_2 ices (Fayolle et al. 2011) and a plethora of minor gases (Le Roy et al. 2015) is a complex process in which volatile minor gases dissolved in the ice may be released once their sublimation temperature is reached, but a substantial portion of them is set free only when the host ice structure sublimates (see, e.g., Collings et al. 2004). Moreover, our knowledge of the structure of the ices and of the desorption and sublimation properties of the relevant volatiles is quite limited at the low temperatures prevailing at the comet surface.

The European Space Agency's *Rosetta* mission has examined comet 67P/Churyumov-Gerasimenko from up close from August 2014 to September 2016, as the comet moved from 3.5 au to perihelion at 1.24 au in mid 2015 and out again up to 3.6 au, when the spacecraft was disposed of on the comet and shut down. In particular the Double Focusing Mass Spectrometer (DFMS) of ROSINA (*Rosetta* Orbiter Spectrometer for Ion and Neutral Analysis, Balsiger et al. (2007)) onboard *Rosetta* was the instrument of choice for *in situ* examination of the sublimation of volatile material. An early result that hinted at the role of species volatility in the sublimation process was the observed difference in coma composition between 67P's northern and southern hemispheres when the comet was still far from the Sun, with more sublimation of the more volatile CO and/or CO_2 relative to water from the southern hemisphere, the colder winter hemisphere at that time, although different surface compositions could have played a role as well (Hässig et al. 2015). Similar volatility effects have been reported by Gasc et al. (2017) on the outbound part of the orbit. A further study by Luspay-Kuti et al. (2015) found a correlation between HCN, CH_3OH, and H_2O, while C_2H_6 follows CO and CO_2, suggesting associations of the minor species with either water ice or with the more volatile CO and CO_2 ices, respectively.

Dhooghe et al. (2017) report the detection of the hydrogen halides HF, HCl, and HBr in the coma. They explain their presence by unprocessed incorporation of interstellar grains in the comet nucleus at the time of formation, since the observed depletion of the hydrogen halides in the gas phase of dense molecular clouds strongly suggests that these halides reside on the surface of the grains in such clouds (see also Kama et al. 2015; Peng et al. 2010; Emprechtinger et al. 2012). The present paper uses the same data set to study the abundances of the hydrogen halides observed by DFMS in the atmosphere of 67P in more detail. Evidence is presented that indicates that the hydrogen halides HF and HCl sublimate not only from the surface but also from dust particles in the inner coma, which thus constitute a distributed gas source (Cottin & Fray 2008) in the coma of comet 67P/Churyumov-Gerasimenko.

2 DISTRIBUTED SOURCES

We follow the definitions introduced by Cottin & Fray (2008) regarding distributed sources. We build a simple model of a distributed source in order to provide the background against which the DFMS observations of the hydrogen halides can be interpreted.

2.1 Comet grain model

The development of water ice envelopes on refractory grains in molecular clouds, and the role of the hydrogen halides therein, has been modeled by Kama et al. (2015) for the case of HCl. Such envelopes start with the formation of water ice; note that water is one of the least volatile species in the molecular cloud gas phase. The hydrogen halides adsorb onto such water ice surfaces as soon as they form. This may at first seem somewhat counter-intuitive, as HF, HCl, and HBr are rather volatile species with sublimation enthalpies of ~30 kJ/mol for HF (Cervinka & Fulem 2017) and ~20 kJ/mol for HCl in the 100–150 K temperature range for the pure species (Inaba & Chihara 1978; Ser & Larher 1990), compared to ~50 kJ/mol for H_2O ice at 150 K (Feistel & Wagner 2007). While the sublimation enthalpies of the hydrogen halides correspond reasonably well to the adsorption energies of hydrogen halide molecules on solid pure hydrogen halide material, the relevant process here is the adsorption onto water ice surfaces. The hydrogen halides are polar diatomic molecules that readily dissolve in water. HCl, for instance, is believed to be ionically dissolved in surface ice following

$$HCl + H_2O \rightarrow Cl^- + H_3O^+,$$

analogous to the solution of hydrochloric acid in water. At low temperatures and low concentrations, there is a significant free energy associated with the adsorption of hydrogen halides (sub-monolayer coverage) onto water ice. The uptake and autoionization of HCl on low temperature water ice has been studied experimentally (Ayotte et al. 2011; Olanrewaju et al. 2011; Parent & Laffon 2005; Park & Kang 2005) for porous amorphous, amorphous, and crystalline water ice surfaces. The process can be interpreted as rapid ionization of HCl at the surface at temperatures as low as 20 K. The surface of the ice becomes disordered as HCl autoionizes and forms contact ion pairs (Olanrewaju et al. 2011). Quantum-mechanical calculations by Svanberg et al. (2000) corroborate this view of the adsorption of HCl onto water ice. They find a 43 kJ/mol binding energy, similar to what is reported by Olanrewaju et al. (2011), plus an additional 21 kJ/mol if one includes the free energy of the ionization, which corresponds to the solvation process, that is, the proton transfer of the hydronium ion to the water matrix (for crystalline ice). Ayotte et al. (2011) find a sticking coefficient of unity below 60 K, indicating that the adsorption process is highly efficient in typical molecular cloud environments. Depending on the degree of ordering of the halogens in the water ice matrix, one can equivalently describe this configuration in terms of water complexes of the form $H_2O{\cdot}HCl$ (formation of hydrates as discussed by Delzeit et al. 1993) which decay as temperature goes up, in a process reminiscent of hydrated minerals (similar to hydrated halite). HF is similarly characterized by ionic adsorption onto water ice, although it is smaller and more easily accommodated in the water ice matrix (Ayotte et al. 2009; Calatayud et al. 2003; Toubin et al. 2003).

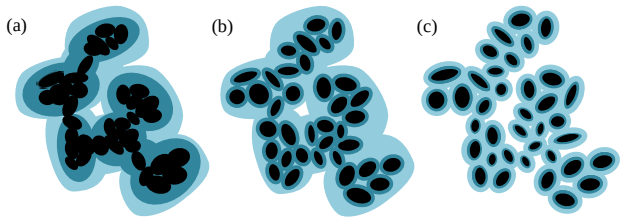

Figure 1. Models of aggregate dust particles. Submicron- to micron-sized refractory subunits (in black) aggregate to form larger dust particles with sizes on the order of 50–100 μm up to the millimetre scale, typically in a hierarchical fashion, represented here by aggregation of subunits first into units with an intermediate size of 5–10 μm. Three situations are described: (a) if the collision time scale is shorter than that of ice deposition, subunits first aggregate and subsequently acquire a water ice mantle with a high content of hydrogen halides (dark blue); later, as the halogens have been removed from the gas phase, a pure ice mantle (light blue) is deposited; (b) if the collision time scale is in between that of halogen-bearing and pure ice deposition, the grains first acquire a halogen-rich mantle before aggregating and then gaining a pure ice envelope. (c) if the collision time is very long, the icy mantles form first and aggregation occurs later on. There must be a smooth transition between these three possibilities. Indeed, the voids between the refractory grains formed in scenario (a) may become filled with halogen-bearing ice after the initial aggregation phase, blurring the distinction with scenario (b). Also, the gradient between halogen-enriched and halogen-poor ice is not so sharp, so that there must be a progressive transition between scenarios (b) and (c) as well. See main text for more details.

The prompt uptake of hydrogen halides by water ice at very low temperature plays a key role in models explaining the observed depletion of the halogens in the gas phase in molecular clouds (Kama et al. 2015). The result is that submicron interstellar refractory dust grains become covered with an envelope of water ice in which hydrogen halides are embedded, with a halogen density gradient that depends on the initial amount of halogen in the interstellar cloud and the speed of halogen and hydrogen halide uptake. As these particles further evolve in a halogen-depleted gaseous environment, they may aggregate, and with time more extended halogen-poor water ice envelopes may develop. Aggregation of such particles then leads to conglomerates as sketched in Fig. 1, held together by the ices and by Van der Waals forces (Hilchenbach et al. 2017). As indicated in the figure, different situations can be expected depending on the mean particle collision time compared to the halogen-rich and halogen-poor water ice deposition times. The aggregates have significant porosity and low cohesion. Their further evolution as they find their way into comets is still largely uncertain. In any case, the detection by *Rosetta*/ROSINA-DFMS of the highly volatile N_2 (Rubin et al. 2015), O_2 (Bieler et al. 2015a), and Ar (Balsiger et al. 2015) indicates that 67P formed at low temperatures and remained cold during its evolution (see also Fulle et al. 2016a). Because of these cold temperatures, together with the reduced mobility and low diffusion coefficients for the ionically dissolved halogens (Delzeit et al. 1993; Wolff et al. 1989), the gradient in halogen content in the icy envelopes must have been preserved.

Many dust particles from 67P are observed to be such conglomerates (Schulz et al. 2015; Hilchenbach et al. 2017). Dust particles are observed by COSIMA after collection on a target plate (Kissel et al. 2007). The particle collection process leads to the loss of all volatile material, given the temperature in the instrument and the time that elapses between collection and analysis. Due to their weak mechanical strength and the volatile removal, a fraction of the particles appears as a "rubble pile" of typically hundreds of micrometres across when first imaged by COSIMA, with constituent refractory units that are somewhat more cohesive, at an intermediate scale around 10 μm or less. Even particles classified as "compact" upon collection are easily broken down into rubble piles after application of mechanical and/or electrostatic forces (Hilchenbach et al. 2017). The atomic force microscope of the MIDAS instrument (Riedler et al. 2007) onboard *Rosetta* has been able to demonstrate that the refractory units themselves are built up hierarchically from subunits of 3 μm down to 0.2 μm (Bentley et al. 2016; Mannel et al. 2016). The submicron size of the smallest subunits is compatible with the size of interstellar dust grains (see, e.g., Westphal et al. 2014; Altobelli et al. 2016). *Rosetta*'s GIADA (Della Corte et al. 2014) and OSIRIS (Keller et al. 2007) instruments have allowed the determination of the dust particle mass spectrum (Rotundi et al. 2015; Fulle et al. 2016c). At the upper end of the spectrum even decimetre- to metre-scale aggregates have been reported (Agarwal et al. 2016; Fulle et al. 2016c).

The desorption of molecules from icy grain mantles can in general be thermally driven or activated by energy deposition of photons or energetic particles (e.g. Collings & McCoustra 2005). In the case of 67P, thermal desorption and photon-driven desorption are most relevant. Desorption does not represent a thermodynamic equilibrium situation, but is a kinetic process. The desorption of H_2O molecules from pure water ice films has been measured experimentally to occur in the range 140–165 K with a peak near 160 K (Collings et al. 2004; Collings & McCoustra 2005); the detailed temperature range depends on the heating rate, the ambient environment, the porosity and surface roughness, and the minor ingredients embedded in the water ice. Collings et al. (2004) distinguish three types of behaviour.

- CO, as an example of a volatile species, with a 7.3 kJ/mol desorption energy much less than that of water (Collings & McCoustra 2005; Luna et al. 2014), experiences a first desorption from a water ice mixture at temperatures of 20–60 K, in agreement with its small desorption energy. A very small molecule like CO can also diffuse into the ice as it is slowly heated. A significant CO fraction escapes from the ice at temperatures around 140 K due to volcano desorption, and around 160 K corresponding to co-desorption of CO with H_2O (Viti et al. 2004).
- Species like CO_2, with a desorption energy of 26 kJ/mol still less volatile than water (Luna et al. 2014) but too large to diffuse into the ice, show multi-layer desorption in a broad temperature range around 80 K, again followed by desorption at 140 and 160 K, as these species are mixed into the ice matrix.
- Finally, species with volatilities comparable to that of water or larger are released in the broad water desorption peak around 160 K.

Sophisticated models of the desorption process have been developed and support the interpretation of the experimental observations (Fayolle et al. 2011). The situation for hydrogen halides is somewhat modified due to their ionic dissolution in the ice. Adsorption of hydrogen halides into the water ice can be viewed as inserting impurities into the ice, substituting water molecules in the ice lattice and increasing the number of point defects with a limited mobility (Bartels-Rausch et al. 2014), which has a stabilizing effect (Delzeit et al. 1993) and can increase the sublimation temperature and constrain diffusion. Experiments show that HCl desorption begins at 115 K, but most of it essentially co-desorbs with H_2O around 170–180 K (Park & Kang 2005; Olanrewaju et al. 2011). As chlorine is released from the water ice matrix, it recombines with hydrogen and sublimates in the form of the hydrogen halide (Olanrewaju et al. 2011; Kama et al. 2015); the same recombinative desorption process is thought to occur for the other halogens.

2.2 Distributed source from aggregate particles

We present a simple model of the sublimation from ice–dust aggregates, coupled to the transport of neutral gas and dust particles in the inner coma, in order to provide a basic description of a distributed source in the inner coma of 67P.

The continuity equation for the flow of a species s through a flow channel in the coma with a cross-section $A(r)$, where r is the coordinate along the channel, is

$$\frac{\mathrm{d}}{\mathrm{d}r} n_\mathrm{s}(r) v_\mathrm{s}(r) A(r) = (S_\mathrm{s}(r) - L_\mathrm{s}(r)) A(r), \quad (1)$$

in which n_s denotes the density of s, v_s is the outward speed of s, and S_s and L_s represent the sources and losses of species s per unit volume and per unit time. If $A(r) = A_0(r/r_0)^\gamma$, with r_0 a reference position, and if the speed is considered constant, Eq. 1 becomes

$$\frac{\mathrm{d}n_\mathrm{s}}{\mathrm{d}r} + \gamma \frac{n_\mathrm{s}}{r} = \frac{S_\mathrm{s} - L_\mathrm{s}}{v_\mathrm{s}}. \quad (2)$$

The power-law relation describing how the flow tube cross-section changes with distance may not be quantitatively correct close to the nucleus. Also the constant speed approximation may not be justified close to the nucleus. Fink et al. (2016) find that water accelerates at 67P out to 10 km cometocentric distance, while other volatiles such as CO_2 do not. The dust particles released from the nucleus are accelerated by the gas flow against gravity, up to the point where the gas drag becomes negligible due to coma gas expansion; the terminal speed depends on particle size.

When applied to the gas coma, the initial conditions are typically taken at the top of the Knudsen layer, i.e. with r_0 slightly larger than the radius of the nucleus. Making abstraction of the actual shape of the 67P nucleus, we take $r_0 = 2$ km. Gas release from 67P is not spherically symmetric due to the two-lobe nucleus geometry, due to the day-night asymmetry, and due to differences in gas production from both hemispheres (see, e.g., Fink et al. 2016). It is possible to use $\gamma = 2$ to describe the expansion in a flow tube far enough from the nucleus so as to avoid non-radial transport due the non-spherical shape of the nucleus and due to longitudinal or latitudinal pressure gradients associated with local variations in gas production. In practice $r/r_0 > 10$ to 20 seems to be required to deal with deviations due to the shape, while $r/r_c > 10$ to 20 is needed to deal with longitudinal or latitudinal pressure gradients, where r_c represents the size of the collisional region, which for 67P is thought to be a few comet diameters at most, depending on comet activity. The $1/r^2$ variation holds well on average as demonstrated, for instance, near the nucleus by the $1/r$ variation observed in line-of-sight integrated densities averaged over a comet-centered annulus by Fink et al. (2016), and farther out by the empirical model of Hansen et al. (2016).

The comet nucleus is described here as a porous mixture of ice and refractory material. A part of the ices sublimates at the nucleus surface and sets free ice-dust entities.

- *Ice*: If such entities have much more ice than dust, they contribute to the gas coma as the ices sublimate, which has been observed to happen mostly close to the nucleus out to a distance of ~10 km (Gicquel et al. 2016; Agarwal et al. 2016). They therefore add to the nucleus's gas production rate Q_g. Since these entities contain only a small number of refractory grains, the fraction of halogen-enriched mantle material is very limited: the sublimating material is mostly halogen-poor ice.
- *Refractories*: The nucleus may also produce entities holding much more dust than ice (actually, this is more likely since the nucleus refractory-to-volatile ratio is $\gg 1$, see below), at a rate denoted here by Q_r. Such entities are held together by strong Van der Waals forces and do not break up. Only the mantles of the grains at their surface sublimate, but since these mantles are only ~1 μm thick while the aggregates have typical sizes of 100 μm or more, the contribution to the gas phase halogen content is small.
- *Ice-dust aggregates*: A limited fraction of the entities produced are ice-dust aggregates ($Q_\mathrm{a} \ll Q_\mathrm{r}$) with a refractory-to-volatile ratio $\delta_\mathrm{a} \sim 1$. Sublimation of the ices leads to a breakup of the aggregates into refractory units of a size intermediate between the aggregate scale and the size of individual refractory grains, in view of the hierarchical structure of the grains. These refractory units are small enough to warm up quickly and porous enough to allow sublimation of the halogen-enriched mantle material around all its constituent grains. This contributes H_2O and hydrogen halides to the gas coma.

The aggregate particles are represented as spheres with a single dominant radius $R_0 = 100\,\mu$m and with low mechanical strength, breaking up into hierarchically structured refractory dust particles with radius $R^* = 5\,\mu$m with stronger cohesion, compatible with the MIDAS and COSIMA measurements (Bentley et al. 2016; Hilchenbach et al. 2017). This dust particle size range has also been confirmed with remote sensing measurements (Hadamcik et al. 2016).

An important parameter is the refractory-to-volatile mass ratio (dust-to-gas or dust-to-ice ratio). This value has been reported for 67P to be $\delta = 4\pm1$ (Rotundi et al. 2015, at 3 au), between 2.4 and 5.3 (Pätzold et al. 2016, 3.5–3 au), ~6 (Fulle et al. 2016c, for the whole inbound pass), 7.5 (Fulle et al. 2017), ~8 (Fulle et al. 2016b, near perihelion). The refractory-to-volatile mass ratio can be computed from the production rates by

$$\delta = \frac{Q_\mathrm{r} + Q_\mathrm{a}\delta_\mathrm{a}/(1+\delta_\mathrm{a})}{Q_\mathrm{g} + Q_\mathrm{a}/(1+\delta_\mathrm{a})}, \quad (3)$$

where the refractory-to-volatile mass ratio δ_a in the aggregates is assumed to be given. The refractory particles are covered with a halogen-rich water ice mantle and embedded in halogen-poor water ice, with mass fractions ξ_m and ξ_i, respectively ($\xi_m + \xi_i = 1$). The aggregates must have a significant porosity p_a, the volume fraction of voids in the aggregate particles.

If both halogen-poor ice and halogen-rich mantle would form a spherical shell of thickness Δ^* around the refractory dust particle units, and since the mass density ρ_i of halogen-poor ice and halogen-rich ice should not differ much, this thickness is related to the refractory-to-volatile mass ratio by

$$\delta_a = \frac{\rho_r}{\rho_i} \frac{1}{(1+\Delta^*/R^*)^3 - 1}. \tag{4}$$

For a refractory density $\rho_r = 2000\,\mathrm{kg/m^3}$ (Fulle et al. 2017) and an ice density $\rho_i = 940\,\mathrm{kg/m^3}$, and with $\delta_a = 1$, a value $\Delta^* = 0.46R^* = 2.31\,\mu$m is found, that is, ice occupies 68 % of the volume of an aggregate. The mass density of an aggregate particle is

$$\rho_a = \frac{1-p_a}{(1+\Delta^*/R^*)^3} \left(\rho_r + \rho_i[(1+\Delta^*/R^*)^3 - 1]\right). \tag{5}$$

For an aggregate porosity $p_a = 0.5$, one finds $\rho_a = 640\,\mathrm{kg/m^3}$; such a porosity and density are compatible with the GIADA measurements (Fulle et al. 2016b, 2017). The situation will be considered here where the halogen-rich mantle contains 12.5 % of the volatile mass of the aggregate ($\xi_m = 0.125$), equivalent to 8.5 % of the aggregate volume; it then has a thickness $\Delta = 0.082R^* = 0.41\,\mu$m.

We now apply the conservation law of Eq. 1 to the aggregate particles. The number of aggregates in a flow tube cross section, $n_a(r_0) = n_a(r)(r/r_0)^\gamma$, must remain constant as no additional aggregates are created and none are destroyed, at least initially. However, the mass of an aggregate with radius $R(t)$ decreases with time and is given by

$$m_a(R(t)) = \rho_a \frac{4}{3}\pi R(t)^3. \tag{6}$$

The illumination energy input is

$$\Phi(t) = (1-a)\alpha\pi R(t)^2 \tag{7}$$

where a denotes the particle's geometric albedo and $\alpha = 340\,\mathrm{W/m^2}$ is the solar constant scaled to a heliocentric distance of 2 au. An albedo of 0.5 is adopted here for these icy aggregates. (Note that albedo values reported for the nucleus surface reflect macroscopic averages; for some exposed pure ice patches, values > 0.40 have been reported (Pajola et al. 2017).) Assuming that the aggregates released by the nucleus are at the ice sublimation temperature, the illumination energy received by the particle is needed solely for providing the latent heat of sublimation of the halogen-poor ice ($C_i \approx 2830\,\mathrm{kJ/kg}$), at least if one ignores heat conduction through the ice and subsequent heating of the mantle and the refractory dust. As the halogen-poor ice sublimates, dust units (still covered with their mantles) are released, so that the effective latent heat of sublimation of the aggregate is

$$C_a = \frac{C_i \xi_i}{1+\delta_a}, \tag{8}$$

which leads to $C_a = 1238\,\mathrm{kJ/kg}$. The aggregate mass evolves following

$$\frac{\mathrm{d}m_a}{\mathrm{d}t} = -\Phi(t)/C_a, \tag{9}$$

so that the aggregate shrinks as its outer layers evaporate, and

$$\frac{\mathrm{d}R}{\mathrm{d}t} = -\frac{(1-a)\alpha}{4\rho_a C_a}, \tag{10}$$

if one adopts a continuous model of aggregate grain evaporation. While a discrete model would be more appropriate, the aggregate-to-grain volume ratio of $(R_0/R^*)^3 = 20^3 = 8000$ seems to be large enough to justify a continuous approximation. The aggregate radius decreases linearly with time. After a time

$$\tau_a = \frac{4\rho_a C_a}{(1-a)\alpha} R_0 \tag{11}$$

the halogen-poor ice has sublimated completely. If the aggregate particle outflow speed v_a is constant, it will have traveled a distance $r_a - r_0 = \tau_a v_a$ before it has disintegrated completely. For the parameters considered here, $\tau_a = 1862\,\mathrm{s}$. With a speed $v_a = 10\,\mathrm{m/s}$ (typical of particles of this size near 2 au (Fulle et al. 2016c)), aggregates reach out to $r_a = 20.6\,\mathrm{km}$. From that point on, $n_a = 0$.

The mass loss from sublimation of the halogen-poor ice in the aggregates deposits material into the gas and dust coma at a rate

$$M_a = -n_a \frac{\mathrm{d}m_a}{\mathrm{d}t}. \tag{12}$$

From the refractory-to-volatile ratio and the mass m_r of a refractory dust particle (without the mantle mass), we then find the rate of creation of free dust particles as

$$S_d = \frac{\delta_a}{1+\delta_a} \frac{M_a}{m_r}. \tag{13}$$

The number of dust particles n_d in the coma can then again be described by Eq. 1, in which this source term appears; there are no losses.

When set free, the dust particles are still covered with their thin halogen-rich mantle and have an initial mass

$$m_{d0} = \frac{4}{3}\pi R^{*3} \left(\rho_r + \rho_i[(1+\Delta/R^*)^3 - 1]\right). \tag{14}$$

The sublimation rate is essentially constant, so that the dust particle mass evolves as

$$\frac{\mathrm{d}m_d}{\mathrm{d}t} = \frac{(1-a)\alpha\pi R^{*2}}{C_m}. \tag{15}$$

The mantle disappears after a time

$$\tau_m = \frac{4\rho_i C_m}{(1-a)\alpha}\Delta, \tag{16}$$

where C_m represents the additional energy that must be supplied for heating a unit mass of mantle material from the halogen-poor ice sublimation temperature to that of the mantle (10–20 K higher) and for the sublimation itself. In addition, some of the heat may be conducted through the thin mantle and be used to heat the refractory dust. A representative value $C_m = 2C_i$ has been adopted here. For the numerical values adopted here, the mantle sublimation time is $\tau_m = 55\,\mathrm{s} \ll \tau_a$. The number n_m of refractory dust particles that are still shedding their halogen-rich mantle is then

found from

$$n_{\rm m} = \frac{1}{v_{\rm d} r^{\gamma}} \int_{r'=r-v_{\rm d}\tau_{\rm m}}^{r'=r} S_{\rm d}(r') r'^{\gamma} {\rm d}r', \tag{17}$$

where $v_{\rm d} = 10\,{\rm m/s}$ is taken as the dust speed; the smaller sublimating dust particles move with essentially the speed of the aggregates (except if they are set free very close to the nucleus where the gas drag can accelerate them). Actively sublimating dust thus travels over $\tau_{\rm m} v_{\rm d} = 0.55\,{\rm km}$ before the mantle is completely lost. Sublimation of mantle material contributes mass to the gas coma at a rate

$$M_{\rm m} = -n_{\rm m} \frac{{\rm d}m_{\rm d}}{{\rm d}t}. \tag{18}$$

There are now two contributions to the number of molecules of species s in the gas coma, apart from the source on the nucleus surface. The first is that from the sublimating ice in the aggregates. Denoting the molecular mass of s by $m_{\rm s}$ and its mass fraction in the ice by $\beta_{\rm si}$, this contribution is

$$S_{\rm si} = M_{\rm a} \frac{\xi_i}{1+\delta_{\rm a}} \frac{\beta_{\rm si}}{m_{\rm s}}. \tag{19}$$

The second contribution comes from the sublimating mantle material and can be expressed as

$$S_{\rm sm} = M_{\rm m} \frac{\beta_{\rm sm}}{m_{\rm s}} \tag{20}$$

where $\beta_{\rm sm}$ is the mass fraction of s in the mantle material. We assume that the species instantaneously acquire the speed of the outwardly expanding gas coma. Let there also be no significant loss of species s inside the region under consideration. The continuity equation for species s then becomes

$$\frac{{\rm d}n_{\rm s}}{{\rm d}r} + \frac{\gamma}{r} n_{\rm s} = \frac{S_{\rm si} + S_{\rm sm}}{v_{\rm g}}, \tag{21}$$

where $v_{\rm g} = 500\,{\rm m/s}$ is the neutral gas speed near 2 au. Below, this continuity equation is applied to an idealized situation where the halogen-poor ice consists of water only and where the mantle consists of chlorine-enriched water ice ($\beta_{\rm H_2O\,i} = 1$, $\beta_{\rm HCl\,i} = 0$, $\beta_{\rm H_2O\,m} = 0.90$, $\beta_{\rm HCl\,m} = 0.10$).

Finally, Eq. 1 can be applied to the purely refractory grains produced by the nucleus as well. For constant speed and in the absence of fragmentation, the density of these refractory grains integrated over the flow tube cross-section does not change with distance.

2.3 Spatial profiles

Figure 2 presents just one example of such a distributed source. Rather than plotting the densities of the species, it is easier to plot $n(r_0/r)^{\gamma}$, which remains constant in the absence of any source or loss. In the example, the gas production from the nucleus at 2 au is $Q_{\rm g} = 20\,{\rm kg/s}$, corresponding to what is observed at 67P near 2 au (Hansen et al. 2016), while the refractory grain production is $Q_{\rm r} = 160\,{\rm kg/s}$ and the aggregate production is only $Q_{\rm a} = 2.5\,{\rm kg/s}$ (see, e.g., Fulle et al. 2016c). With $\delta_{\rm a} = 1$ and these production rates, one finds $\delta = 7.6$, which matches the observed values pretty well. The top panel in Fig. 2 shows how the number of aggregates (with an initial diameter of 200 μm, in blue) remains constant until $r_{\rm a} = 20.6\,{\rm km}$, after which

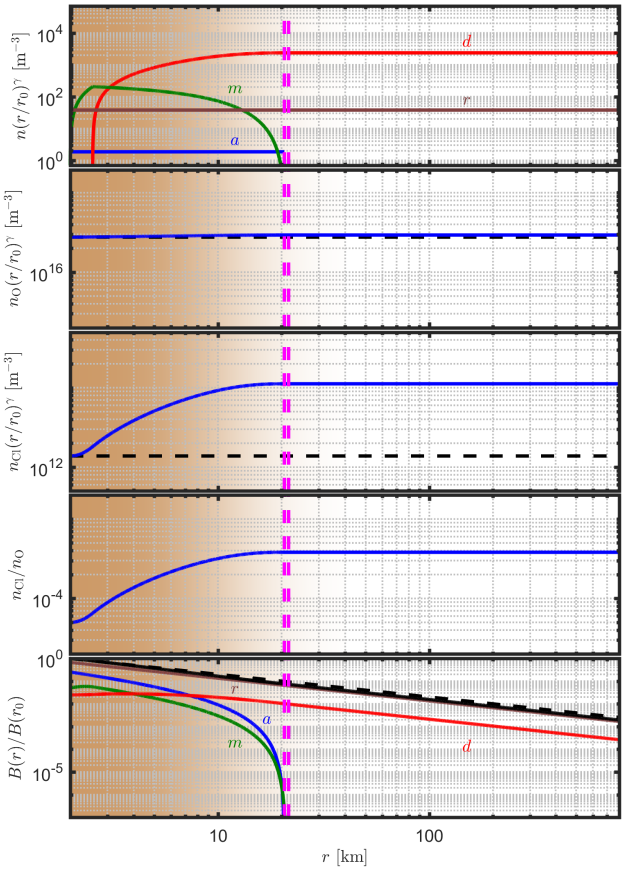

Figure 2. A simple model of a distributed source for chlorine in 67P at 2 au. From top to bottom: scaled number densities of aggregates (blue), refractory particles set free from the aggregates, with sublimating mantle (green) and without (red), and refractory particles released from the nucleus (brown), as a function of cometocentric distance; radial profile of the elemental O density in the inner coma (solid line) compared to the density from gas production at the nucleus surface only (dashed line); idem for the elemental Cl density; profile of the $n_{\rm Cl}/n_{\rm O}$ ratio; relative brightness integrated along the line of sight for a spherical coma (solid black line) with contributions from aggregates (blue), refractory particles with (green) or without mantle (red), and refractory particles from the nucleus (brown), together with a $1/r$ dependency (dashed line) for reference. The leftmost vertical line corresponds to the distance out to which aggregates sublimate; the rightmost vertical line gives the extent of the distributed source. See main text for more details. The shading indicates that the model approximation may be poor close to the nucleus where the flow speed is not necessarily constant and where the cross-section of a flow tube might not need to follow a power law as a function of distance along the streamline.

they have disintegrated due to sublimation (leftmost vertical dashed line). In reality, a spectrum of aggregate sizes is expected. Each aggregate size corresponds to a characteristic distance, with larger aggregates having longer lifetimes but slower outward speeds, so that the characteristic distance would remain in the order of tens of kilometers. The characteristic distance obviously depends also on heliocentric distance: closer to the Sun, sublimation proceeds faster, but gas production is higher and hence the outward speeds will be higher as well. As the aggregates

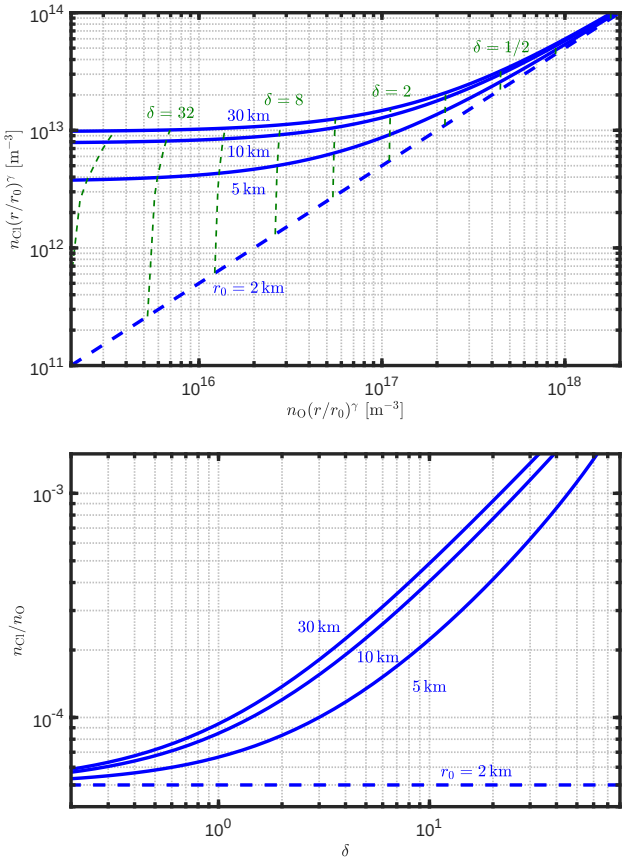

Figure 3. Top: Halogen versus oxygen elemental densities at selected distances from the nucleus for constant refractory and aggregate production rates but variable neutral gas production rates on the nucleus surface, resulting in a varying refractory-to-volatile ratio δ. Bottom: Profiles of the $n_{\rm Cl}/n_{\rm O}$ ratio at selected distances from the nucleus as a function of δ. The ratios are plotted for different distances from the nucleus; the dashed line corresponds to r_0, the position at which the aggregates are released and start sublimating. See main text for interpretation.

lose mass, they progressively liberate units, consisting of refractory particles still covered with a mantle (10 μm diameter, in green). These units are small enough to warm up quickly and porous enough to allow all mantle material to sublimate, leading to dessicated refractory units (in red). While the number of mantle-coated refractory units initially increases, the ones liberated first have lost their mantle by the time they reach $r_{\rm m} = r_0 + \tau_{\rm m} v_{\rm d} = 2.55$ km. The bare refractory particles thus appear from that distance on. Dust particles with sublimating mantles are found out to a distance $r^* = r_0 + \tau_{\rm a} v_{\rm a} + \tau_{\rm m} v_{\rm d} = 21.2$ km, which one could define as the size of the distributed source (rightmost vertical line). In this example it is assumed that the refractory grains escaping directly from the nucleus are all of the same size as the icy aggregates; they contribute to the dust coma brightness. The density of the latter particles, integrated over the flow tube cross-section, is constant (in brown). The second and third panels show the elemental number densities of oxygen and chlorine. In the model the gas sublimating from the nucleus has a low halogen abundance $n_{\rm Cl}/n_{\rm O} = 5 \times 10^{-5}$ (corresponding to $\beta_{\rm HCl\,g} = 0.0001$), the ice mixed in with the dust particles contains no halogens, while the dust mantle material has a high relative chlorine abundance of 0.05 (corresponding to $\beta_{\rm HCl\,m} = 0.10$). Consequently, the oxygen radial profile is dominated by the neutral gas produced at the surface, with the contribution from sublimation of the halogen-poor ice in the aggregates and of the dust particle mantle material being fairly minor. The distributed source for water contributes in the present example a fraction

$$\frac{n_{\rm H_2O\,a}}{n_{\rm H_2O\,g}} = \frac{Q_{\rm a}}{Q_{\rm g}} \frac{\xi_{\rm i}\beta_{\rm H_2O\,i} + \xi_{\rm m}\beta_{\rm H_2O\,m}}{\beta_{\rm H_2O\,g}(1+\delta_{\rm a})} \approx \frac{Q_{\rm a}/Q_{\rm g}}{1+\delta_{\rm a}}, \tag{22}$$

which amounts to 6 % of the water sublimating from the nucleus (consistent with Fulle et al. 2016a). However, the relative importance of the chlorine distributed source is much higher, the total halogen content being

$$\frac{n_{\rm HCl\,a}}{n_{\rm HCl\,g}} = \frac{Q_{\rm a}}{Q_{\rm g}} \frac{\xi_{\rm i}\beta_{\rm HCl\,i} + \xi_{\rm m}\beta_{\rm HCl\,m}}{\beta_{\rm HCl\,g}(1+\delta_{\rm a})} \approx \frac{Q_{\rm a}/Q_{\rm g}}{1+\delta_{\rm a}} \frac{\xi_{\rm m}\beta_{\rm HCl\,m}}{\beta_{\rm HCl\,g}}, \tag{23}$$

or ~8 times that in the gas released from the nucleus. The halogen-to-oxygen ratio (Fig. 2, bottom panel) gives therefore a clear indication of the size of the distributed source and of its importance.

While in the above model the fragmentation of the aggregates controls the delayed release of the mantle material and thus is a crucial element in explaining the size of the distributed source, fragmentation also causes an increase of the total reflecting grain surface so that one may wonder whether this is not in conflict with the observed decreasing coma brightness profile (see, e.g., the background brightness in Gicquel et al. 2016). This is not the case. The effect of fragmentation on the brightness profile is limited because the aggregates constitute only a small fraction of all dust escaping from the nucleus ($Q_{\rm a} \ll Q_{\rm r}$). Moreover, upon fragmentation of the icy aggregates into the units, the volatile fraction $1/(1+\delta_{\rm a})$ sublimates. Also, aggregates and dessicated units do not have the same density (640 and 2000 kg/m^3, respectively) nor the same albedo (0.50 and 0.05, respectively). Taking all these elements into account, the effective reflecting surface of the fragments is, in the present example, actually smaller than that of the parents. The bottom panel in Fig. 2 gives the total relative dust coma brightness $B(r)/B(r_0)$ integrated along the line of sight for the particular case of a spherical coma (solid black line). For reference, the dashed line shows the $1/r$ dependence that is expected for a spherically expanding set of particles. The fine refractory grains escaping from the nucleus follow that trend (in brown). The contribution from the aggregate grains (blue) is the largest initially, but decreases slightly faster than $1/r$ as the aggregates shrink and disappear altogether at the distance $r_{\rm a}$. The refractory particles with a sublimating mantle (in green) have a contribution that initially is flat, and then starts to decrease out to distance r^*. The refractory particles that have been set free from the aggregates and that have lost their mantle (red) contribute in an increasingly larger proportion to the total brightness, until distance r^*, from where they follow the $1/r$ behaviour. While the total brightness might slightly increase above the $1/r$ level in the first few kilometers from the nucleus surface (where deviations from spherical symmetry are likely to occur anyhow), it has a slightly steeper decrease $B(r) \sim 1/r^{1.2}$ farther out in the distributed source region (strongly depending on the size distributions of the icy aggregates and of the refracto-

ries originating on the nucleus), and changes to $B(r) \sim 1/r$ beyond r^*.

Obviously, this is a very simplified steady-state model. The actual profiles depend on the full mass distribution of the particles responsible for the distributed source. Close to the nucleus, the constant velocity approximation and the assumption of a flow tube cross-section that grows following a power-law of the distance along a streamline may not be valid, as indicated by the shading in Fig. 2. Note that the coma has never been sampled so close to the comet by *Rosetta*, except immediately prior to the end of the mission. While realistic values have been adopted here for the model parameters, reflecting the observed dust and gas properties, some of the parameters are ill-constrained. A distributed source size of several tens of kilometers, changing with comet activity, appears plausible.

At some distance from the comet the larger escaping particles in the dust coma are expected to be distributed rather uniformly as a consequence of mixing as the particle speeds are small (compared to the gas) and show a certain spread. Variations in aggregate production with longitude, latitude, and with time, therefore average out and one can consider the aggregate production rate to be rather constant over the duration of a single comet rotation. The gas escaping from the nucleus, on the contrary, exhibits a strong diurnal variation. It is therefore interesting to examine what happens if the gas production rate Q_g changes for fixed aggregate and refractory production rates Q_a and Q_r. Figure 3 (top) plots the correlation between the halogen and oxygen densities $n_{Cl}(r_0/r)^\gamma$ and $n_O(r_0/r)^\gamma$ at increasing cometocentric distances as δ varies; Fig. 3 (bottom) plots the n_{Cl}/n_O ratio. The relative abundance of the halogens grows with increasing δ. One can consider two extremes. If there is much more neutral gas than aggregates and refractories ($\delta \to 0$), the contribution of the distributed source is negligible and the halogen and water densities are linearly related, as in the right of Fig. 3 (top). If, however, there is very little neutral gas compared to aggregates ($\delta \gg 1$) and one is sufficiently far from the nucleus, the amount of halogens is dominated by the distributed source so that the total halogen abundance becomes nearly independent of the amount of water, as seen on the left of Fig. 3 (top).

3 OBSERVATIONS AND INTERPRETATION

The *Rosetta* mission to 67P offered an unprecedented opportunity to sample the volatiles in the inner coma of a comet up close with ROSINA-DFMS. This is extremely difficult, if not impossible, to do with remote sensing from Earth because of the limitations on angular and hence spatial resolution (see, e.g., Opitom et al. 2015, for a recent example). Additionally, remote sensing observations are limited to species with strong transition lines, possibly interfering with the same molecules in the Earth's atmosphere, and give line-of-sight integrated results which have to be inverted using a coma model to obtain spatial density profiles.

3.1 ROSINA/DFMS data set

We have studied the halogen-bearing compounds in the coma with DFMS on 67P's inbound journey during four periods, while the gas production increased towards perihelion and as the comet's subsolar latitude moved from the northern to the southern hemisphere, using the same data set as Dhooghe et al. (2017).

The most significant fluxes of coma neutrals into the instrument, including halogen-bearing gases, are observed when the spacecraft is close to the comet and/or when the comet is active (close to perihelion). High mass resolution DFMS data with sufficient signal-to-noise ratio have been obtained during the comet's inbound journey towards perihelion. Special emphasis is given to the time periods indicated in Fig. 4: (A) the 10 km orbit period when *in situ* neutral densities were obtained with high signal-to-noise ratio, (B1 and B2) the close flybys at 8 km and 13 km, (C) the post-equinox period when the southern hemisphere became the dominant gas source, and (D) the period around perihelion when comet activity ensured significant flux despite *Rosetta*'s larger distance from the nucleus. We have eliminated all data during and shortly after significant spacecraft attitude changes which might lead to spacecraft outgassing (Schläppi et al. 2010).

The overall data analysis procedure has been described specifically for the halogen-bearing compounds by Dhooghe et al. (2017). These authors have established that most, if not all, of the HF, F, HCl, Cl, HBr and Br fragment ions detected by DFMS can be attributed to their respective hydrogen halide parents HF, HCl, and HBr. The analysis presented here concerns HF and HCl, since bromine was only detected in significant quantities during period A when *Rosetta* was close to the nucleus.

3.2 Factors of variability

Rosetta has observed 67P under a variety of circumstances. It is not straightforward to compare coma measurements acquired at different distances from the sun, at different distances from the comet, as a function of changing season and of the comet's daily rotation, and depending on the spacecraft longitude and latitude above the nucleus. We have therefore sorted the data during the four observation periods (A, B1 + B2, C, D) according to all relevant parameters:

- *Total gas production rate*: This parameter is dealt with by considering the elemental abundance ratios F/O and Cl/O of the halogens relative to oxygen, where oxygen serves as a reference for the coma gas since it is part of all main coma constituents. If the hydrogen halide sublimation would be proportional to the total gas production, as one would expect if both occur only on the nucleus surface, and if the total gas production is represented well by the oxygen abundance, variations in gas production rate should cancel in numerator and denominator, leaving the ratio constant. The elemental abundances of the halogens are computed from F/O = HF/O, Cl/O = ($H^{35}Cl$ + $H^{37}Cl$)/O, and Br/O = ($H^{79}Br$ + $H^{81}Br$)/O, while the O abundance is inferred from the H_2O, CO, CO_2, and O_2 that is detected by DFMS, which constitute the majority of the volatiles in the coma (Le Roy et al. 2015; Bieler et al. 2015b).
- *Distance from the Sun*: Each period corresponds to a different heliocentric distance, thus a different level of illumination and thermal input. Within each period, the solar flux variation remains below 20 %. Note that the effects of

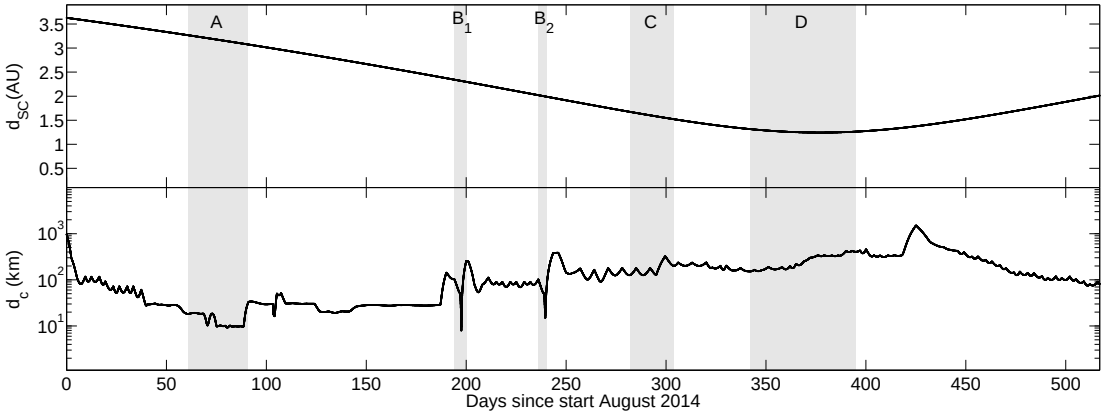

Figure 4. Sun-comet and comet-spacecraft distance for the periods of interest. The plot covers 1/8/2014 to 31/12/2015. The shaded areas indicate the periods (A) close to the comet, 1–31/10/2014, (B1 and B2) the close flybys on 14/2/2015 and on 28/3/2015, (C) post-equinox between 10/5/2015 and 1/6/2015, and (D) around perihelion between 9/7/2015 and 31/8/2015.

heliocentric distance are to a large extent already taken into account by addressing the effects of total gas production rate, but perhaps not all. In particular, if volatile release from icy grains plays a role, the thermal history of the grains, the grain size distribution, and the grain speeds may be affected by the distance from the sun in a more complicated fashion.

• *Phase angle*: Each period is characterized by a relatively constant phase angle: around 90° for period A, around 90° for flyby B1 with a brief dip down to 0° at closest approach, around 75° for B2 with a dip to 40° during closest approach, around 70° for C, and around 90° for most of period D, going down to 70° during the last few days. Given the success of simulations based on the irregular nucleus shape and a description of gas emission at the surface (Bieler et al. 2015b; Fougere et al. 2016), the observed density variation with phase angle is expected to be fairly smooth, leading to limited variations within each period (by a factor of 2 at most), except immediately before and after closest approach during flyby. Moreover, the phase angle effect should cancel out when considering F/O or Cl/O ratios.

• *Latitude*: Because of the orientation of the comet rotation axis relative to its orbital plane and the ensuing seasonal effects, differences in sublimation conditions and variations in surface composition with latitude cannot be excluded (Le Roy et al. 2015; Hässig et al. 2015). We have therefore binned the observations in three groups: *southern hemisphere* for spacecraft latitudes $[-90°, -30°]$, *equatorial* for latitudes $[-30°, +30°]$, and *northern hemisphere* for latitudes $[+30°, +90°]$. Note that the spacecraft latitudes give only a rough indication of where the volatiles are released from the surface, given the large DFMS field of view and the broad solid angle over which sublimating particles escape from the surface.

• *Longitude*: As the comet rotates in about 12 hours, while the spacecraft is moving very slowly relative to the co-rotation speed at *Rosetta*'s cometocentric distance, all longitudes are scanned consecutively. Because of the nucleus geometry and the activity variation across the surface, longitude has an important effect on the abundances measured. These effects may in part be compensated for by considering the ratios, but compositional differences or other effects with longitude cannot be excluded *a priori*. The data set is sufficiently rich so that it covers multiple comet rotations in each period or latitude bin, with as a sole exception the hours surrounding closest approach during the flybys.

• *Cometocentric distance*: As already discussed in Section 2, sufficiently far from the nucleus the coma expansion can be approximated by an inverse-square distance law ($\gamma = 2$). It appears that this law holds pretty well on average (Hässig et al. 2015); also models reproduce this behaviour for most species, at least over the distance range covered by *Rosetta* (Bieler et al. 2015b; Fougere et al. 2016). We have therefore multiplied all measured abundances with the distance squared, so as to facilitate the visualization of any deviations from $1/r^2$ expansion, with the same caveat regarding unwarranted application of this scaling close to the nucleus. Note that the halogen-to-oxygen ratios considered here are independent of the specific expansion law for the flow tube in which observations are collected, since the same scaling is applied to numerator and denominator.

There are also a few instrument- or spacecraft-related effects that have been accounted for.

• When presenting measured densities, the analysis here is limited to data for which the comet is fully within the field of view. However, when presenting ratios, a somewhat broader data selection is used for which at least part of the comet is within the field of view, as the implied observed density reduction factor cancels from numerator and denominator of the ratio.

• The measured densities have been corrected by the cosine of the off-pointing angle, that is, the angle between the instrument viewing direction and the direction of the comet's centre of mass. Note that, in all cases where the comet is fully or partially in view, the off-pointing angle remains rather small, so that this is only a minor correction.

• Another possible factor of variability for HF is the potential presence of a fluorine background of spacecraft origin (Schläppi et al. 2010). Efforts have been made to correct the

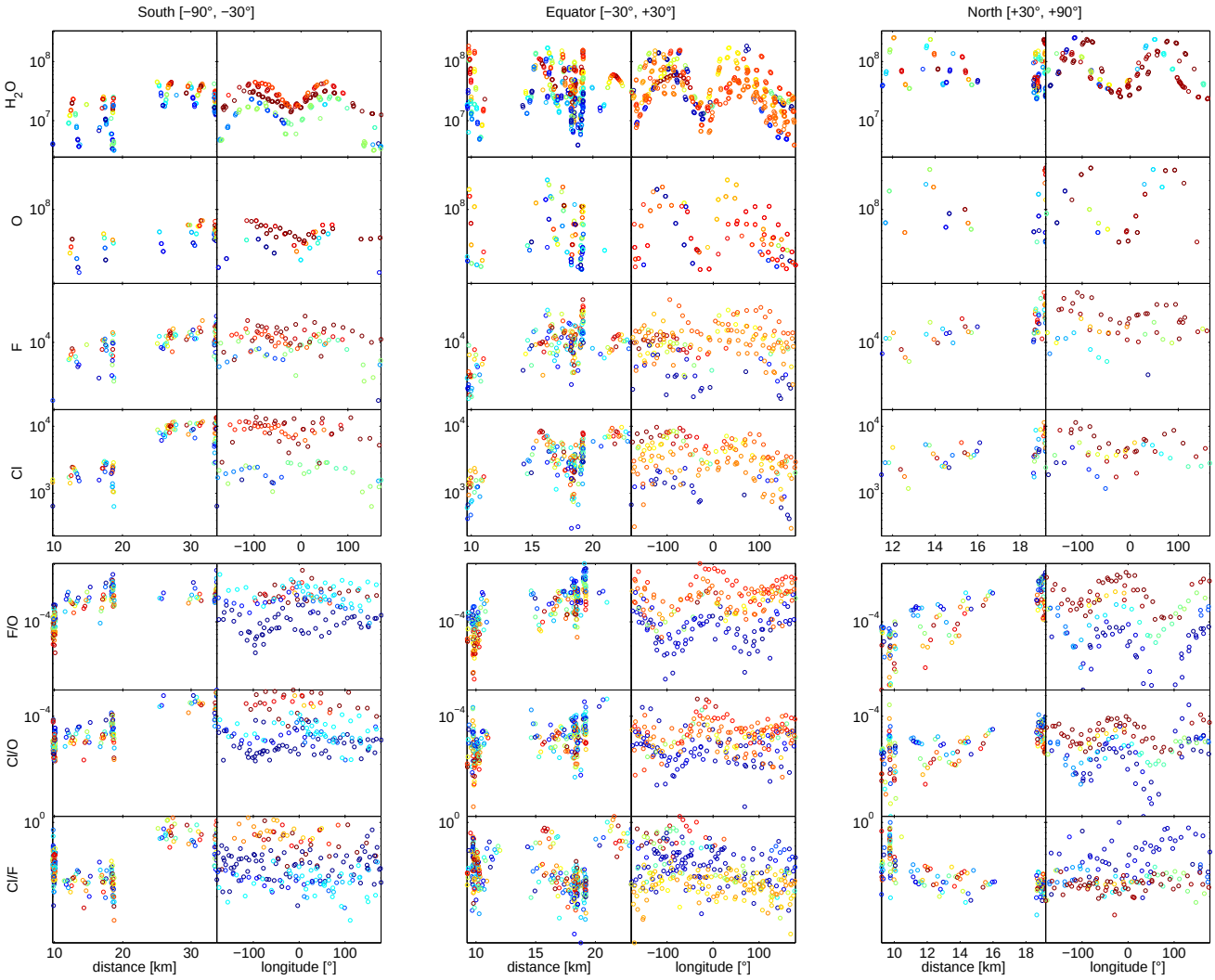

Figure 5. DFMS densities and density ratios for period A. Densities are given in arbitrary units, scaled by distance squared when the full comet was in the field of view and density ratios when at least part of the comet was in the field of view. Plots as a function of distance are colour-coded by longitude, while plots as a function of longitude are colour-coded by distance.

observations for this background, but the background estimation may have been inaccurate. For chlorine this problem may be present as well, but to a lesser extent.

3.3 Analysis of each time period

Figures 5–9 plot, for each period and each latitude bin, the element abundances and the ratios as a function of altitude. In doing so, longitude is used as colour code, with the colour code going up/down 4 times over a full rotation. The figures also plot the abundances and the ratios as a function of longitude using cometocentric distance as colour code. This plot format permits separation of the element abundance ratio dependencies on each of the parameters discussed above.

Consider, for instance, the centre column in Fig. 5 that summarizes data gathered over the equator during period A. The scaled density of H_2O, the species that DFMS measures most often and is thus most appropriate to make this kind of plots, shows no particular trend with distance. The colours indicate the phase of the daily rotation, with blue corresponding to daily minima and red to the maxima. The plot of the H_2O density as a function of longitude shows the daily variation pattern in detail, with at least one order of magnitude difference between minimum and maximum. The colours correspond to the cometocentric distance; no particular trend is visible. A similar picture is obtained for the O element abundance obtained from the H_2O, CO, CO_2, and O_2 abundances. Note that there are less data points as the O abundance is interpolated to the times of F and Cl measurements, and requires nearby measurements of CO, CO_2, and O_2. For F and Cl, however, the picture is different. For both halogens, the scaled densities increase with distance over the 10 to 35 km range. They both show the daily variations. It is particularly striking how the density curves as a function of longitude corresponding to measurements close to the comet (blue) are systematically below the ones obtained farther away (red). Note that all the measurements during this time period were obtained at a phase angle near 90° (mostly terminator orbits). The observed increase with distance therefore cannot be ascribed to changes in latitude, longitude, or phase angle. These density increases

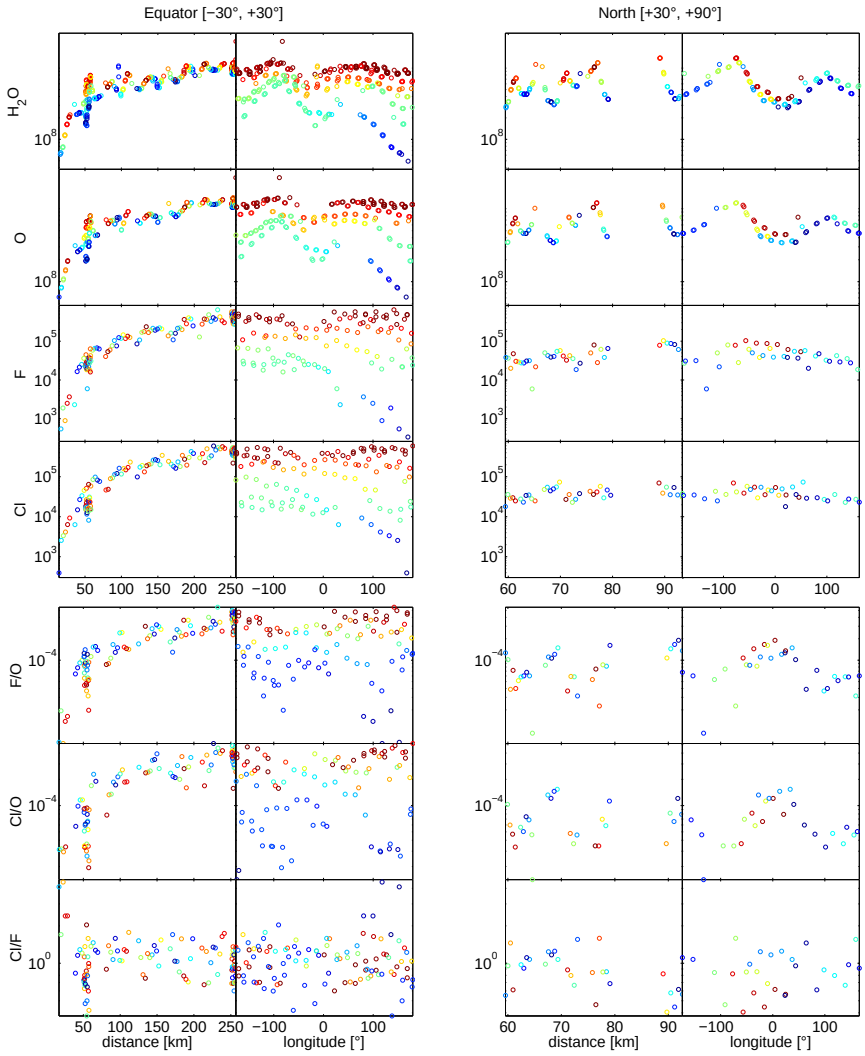

Figure 6. DFMS densities and density ratios for period B1. See caption of Fig. 5 for further explanations.

could, however, be due to an overall change in gas production rate with time, since the spacecraft moved away from the comet near the end of this time period in preparation of the Philae release and landing, i.e. there is a certain correlation between time and distance in the period A data set. It is therefore important to look at the n_F/n_O and n_{Cl}/n_O ratios, which represent the halogen content after normalization with respect to the overall gas production. These ratios are found to increase with distance as well (clear for n_F/n_O, somewhat less for n_{Cl}/n_O). Since the amplitude of the daily variation of the halogens is less than that of the bulk gas, the ratios are at a minimum (maximum) where the O element abundance is maximal (minimal). The colour code again indicates a systematic variation with distance, both for n_F/n_O and n_{Cl}/n_O. A similar behaviour is seen in the southern and northern hemispheres. In conclusion, there is a clear increasing trend in the F and Cl content of the coma gas in the 10–35 km distance range when the comet was at ~3.2 au, that cannot be ascribed to simultaneous changes in other parameters.

Figures 6 and 7 show the data for the B1 flyby covering a range of 15–250 km and for the B2 flyby covering 30–90 km. Closest approach happened at equatorial latitudes. For B1, closest approach actually occurred at longitudes corresponding to minimum gas production, so that the density value obtained there must be interpreted with caution. For B2, the longitude coverage near closest approach was also incomplete. Especially for B1, there is a clear distance dependence, even if one ignores all data taken below 50 km. The densities of the daily variation pattern systematically rise with distance. At closest approach the phase angle is minimal; moving towards higher phase angles is expected to reduce the measured scaled densities, while the opposite is observed: The densities increase for all species or elements (H_2O, O, F, Cl). Both flybys present a similar behaviour, although B1 has a minimum phase angle around 0° and B2 around 40°. The DFMS instrument was kept pointing towards the comet during the flybys. With its 20° × 20° field of view, it keeps the whole comet in view, perhaps only marginally at the flyby altitudes of 10–15 km, but certainly above 30 km. The flyby speed is on the order of a few m/s compared to the gas outflow at 0.5–1 km/s, so that there is no significant aberration effect. Local topography might be responsible for non-spherical outflow ($\gamma \neq 2$), but only close

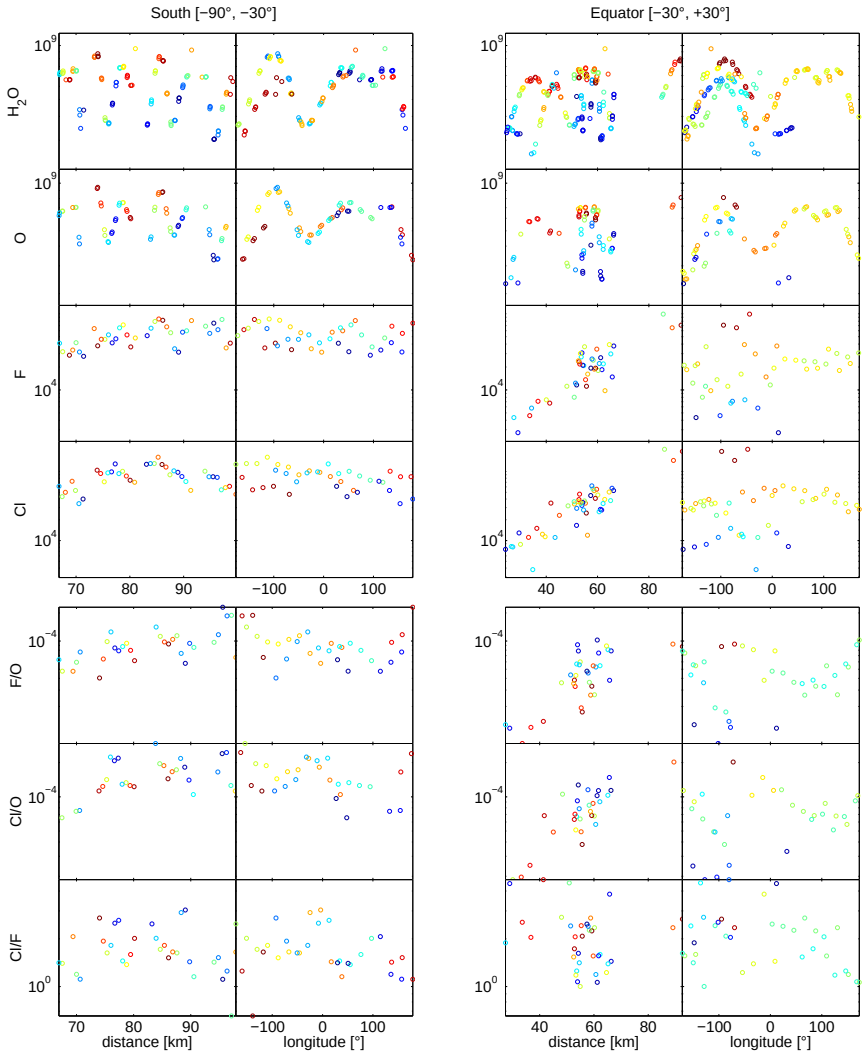

Figure 7. DFMS densities and density ratios for period B2. See caption of Fig. 5 for further explanations.

to the comet, while we observe the density increase up to and beyond 200 km. The major reason for non-spherical outflow, namely the fact that sublimation occurs mostly at the day side so that the coma expands to fill the night side, should actually lead to a faster decrease of the densities ($\gamma > 2$) with distance. During a flyby, however, *Rosetta* is not only scanning radial distance, but its latitude changes simultaneously. An apparent anomalous density increase would be observed if *Rosetta* moves from latitudes with predominantly $\gamma > 2$ towards latitudes with predominantly $\gamma = 2$, even over a period of several comet rotations. Additionally, if *Rosetta* is close to the comet and if the outflow is highly non-radial (which may very well be the case close to the comet in view of the highly non-uniform outgassing patterns seen close to the nucleus by VIRTIS (Fink et al. 2016)), DFMS might miss part of the outflowing gas despite its large field of view, which would lead to the detection of abnormally low densities. One therefore cannot draw any firm conclusions from scaled density plots alone. Even though the number of O atoms (contained in H_2O, CO, CO_2, and O_2) in a spherical shell with unit thickness sometimes seems to increase with distance, the number of halogen atoms does so more rapidly, as n_F/n_O and n_{Cl}/n_O rise with distance as well. The amplitude of the daily halogen density variation progressively decreases farther away from the nucleus.

Period C contains data taken at larger distances, see Fig. 8. Only for the equatorial data, covering 130–200 km, is there a hint of an increase of the O, F, and Cl densities and of the n_{Cl}/n_O ratio with distance. While the daily modulation is clearly visible in the bulk gas, it is essentially absent in the halogen densities.

Period D shown in Fig. 9 actually consists of two time periods, one before and one after perihelion, as the spacecraft moves from around 200 km to around 400 km from the comet. As a consequence of sorting the data in the three latitude bins, the data in these bins consist of two periods a few weeks apart. Note the asymmetry in gas production between the hemispheres for O with 10 times more outgassing in the southern than in the northern hemisphere. The asymmetry is much smaller for F and Cl. The daily density variation is visible out to 400 km also for the halogens, though the modulation is weak. The amplitude of variation for water decreases with distance. While the plots show clear density increases for all species between 200 and 400 km, this can

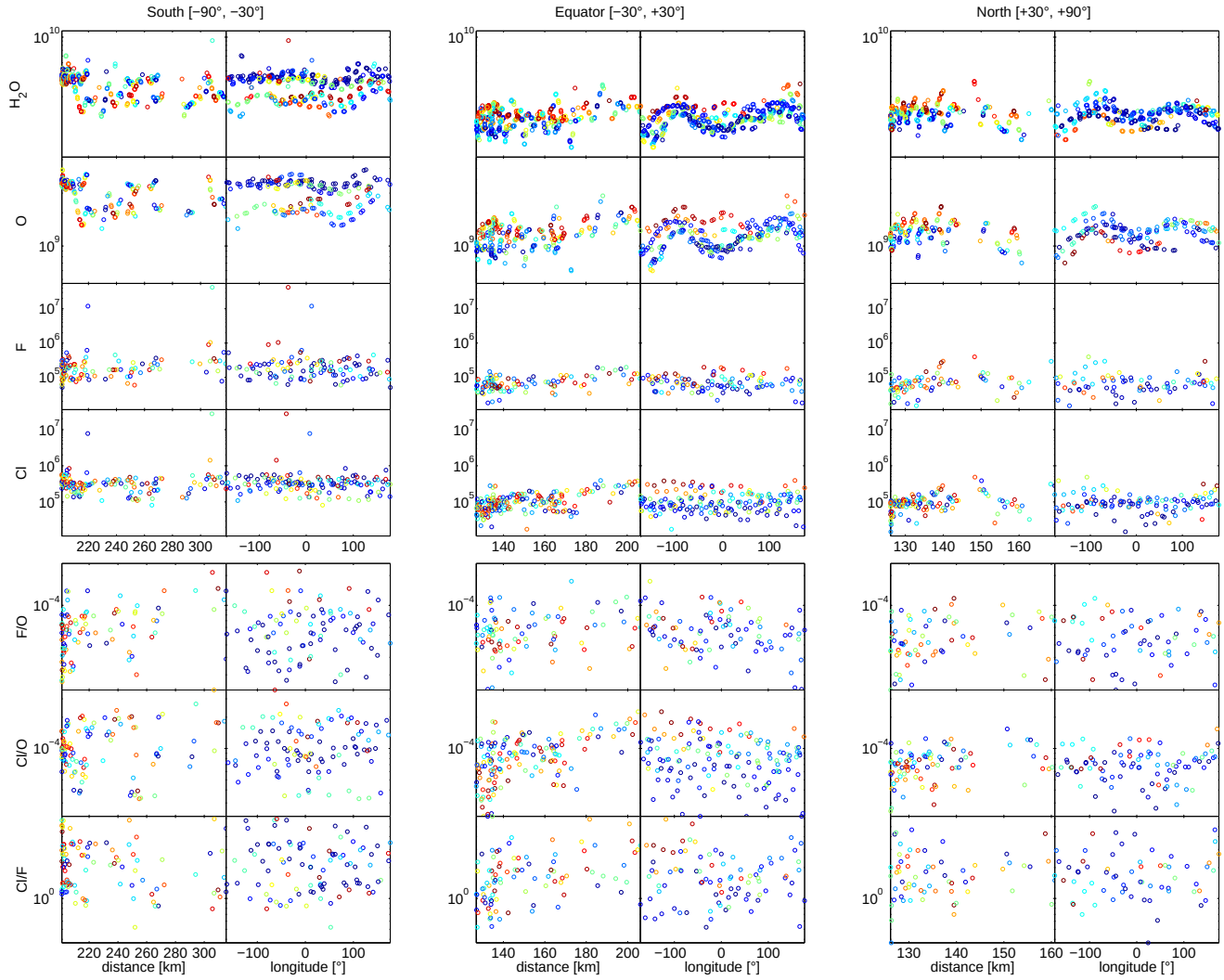

Figure 8. DFMS densities and density ratios for period C. See caption of Fig. 5 for further explanations.

(partly) be due to a change in gas production rate, which effectively peaked two weeks after perihelion. Looking at the ratios, there is clear evidence for an increase in n_F/n_O and n_{Cl}/n_O only in the northern hemisphere. An unknown factor, however, may be the variability in the dust-to-gas production ratio.

3.4 Discussion

The data presented above can be compared with the results from the model introduced in Section 2 while not forgetting the limitations of that model. A steady state model can indeed be used to describe the coma gas, since the gas residence time within 500 km distance is on the order of 1000 s, while the typical changes in coma gas production are on the order of a few hours (a fraction of the daily variation, with 67P's day lasting about 12 hours). For the dust, the residence time is typically an order of magnitude longer, but due to the spread in grain velocities the dust environment tends to become more uniform. In the absence of sources and losses, the F, Cl, and O element abundances must vary inversely with the square of the distance (except close to the nucleus) so that their ratios are constant. It is known that there is no significant loss of the hydrogen halides through photo-dissociation as the HF and HCl photo-dissociation length scales far exceed the cometocentric distances considered here; photo-destruction of the main oxygen-bearing species is a similarly slow process so that relatively little oxygen is lost (Huebner & Mukherjee 2015). Being close to the nucleus, losses through charge exchange, electron impact ionization, and ion-neutral reactions are thought to be of limited importance (Vinodkumar et al. 2010; Nilsson et al. 2015; Fuselier et al. 2015). Therefore, $r^2 n_F$, $r^2 n_{Cl}$, and $r^2 n_O$, as well as the ratios n_F/n_O and n_{Cl}/n_O, should remain constant unless there are additional sources inside the coma. The analysis of all time intervals individually shows unambiguous increases of the scaled Cl and F densities and of the n_F/n_O and n_{Cl}/n_O ratios with distance in all instances where a considerable distance range was covered and/or data close to the nucleus were collected. There must therefore be a source.

There is no single-step bond-cleaving process by which HF or HCl can be created from a possible parent molecule. One could possibly unlock F or Cl from a parent and create

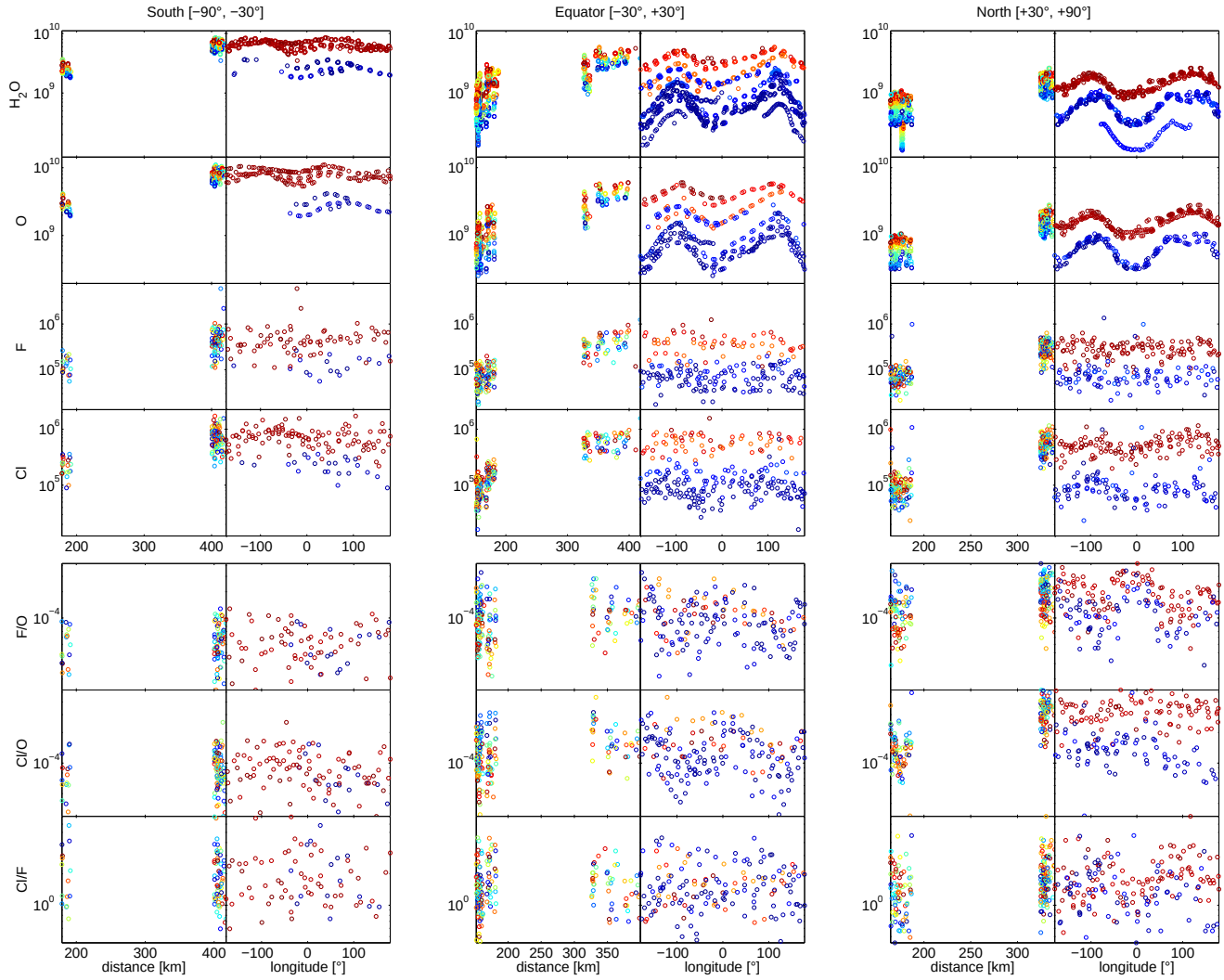

Figure 9. DFMS densities and density ratios for period D. See caption of Fig. 5 for further explanations.

the hydrogen halide by solar wind proton impact, but this would be fairly rare. Also, there is no solar wind present for some of these observations (Nilsson et al. 2017). Moreover, we have not detected any other halogen-bearing neutral at concentrations that can explain the observed increase in the halogen-to-oxygen ratio with distance (see also Le Roy et al. 2015). The presence of organohalogens in 67P has been reported recently by Fayolle et al. (2017), but in insufficient amounts to be able to contribute significantly. Therefore, the source cannot be a secondary source, so it has to be a distributed source (Cottin & Fray 2008): its origin lies in the sublimation of HF and HCl from icy dust.

Figure 10 attempts to summarize how the n_F/n_O, n_{Cl}/n_O, and n_{Cl}/n_F ratios depend on cometocentric distance for southern, equatorial, northern and all latitudes. One has to be very careful when interpreting this plot, since the size of the distributed source is expected to change due to decreasing grain lifetimes towards perihelion as a consequence of more intense insolation and attendant higher grain temperatures, but also due to increased grain speeds from the drag by a faster neutral gas flow, and possibly due to changes in the grain size distribution (Lien 1990; Rubin et al. 2011; Rotundi et al. 2015; Fulle et al. 2016c). Also, the dust-to-gas production ratio may change between the different time periods. The increases in halogen content seem to extend out to somewhere between 20 and 200 km, although a precise value is hard to pinpoint. The n_F/n_O and n_{Cl}/n_O ratios are much higher in the distributed source than in the gas from the comet surface. These findings are in agreement with the model presented earlier.

The observations also hint at a distributed source for the oxygen-bearing species. In particular the profiles $r^2 n_{H_2O}$ for water molecules and $r^2 n_O$ for the overall oxygen element density seem to increase for event A (south), B1 (equator), B3 (equator), D (south, equator, north), while no significant trend is observed for event A (equator), B1 (north), B2 (south, equator), B3 (south, north); the other cases cover a too limited range in distance to draw any conclusion. Nowhere a decreasing trend is observed, despite the expected expansion with $\gamma > 2$. As already mentioned, one should be careful in drawing conclusions from scaled density profiles obtained from a spacecraft moving in a coma where γ changes with comet latitude and longitude, or where the outflow might be non-radial. Note also that these observa-

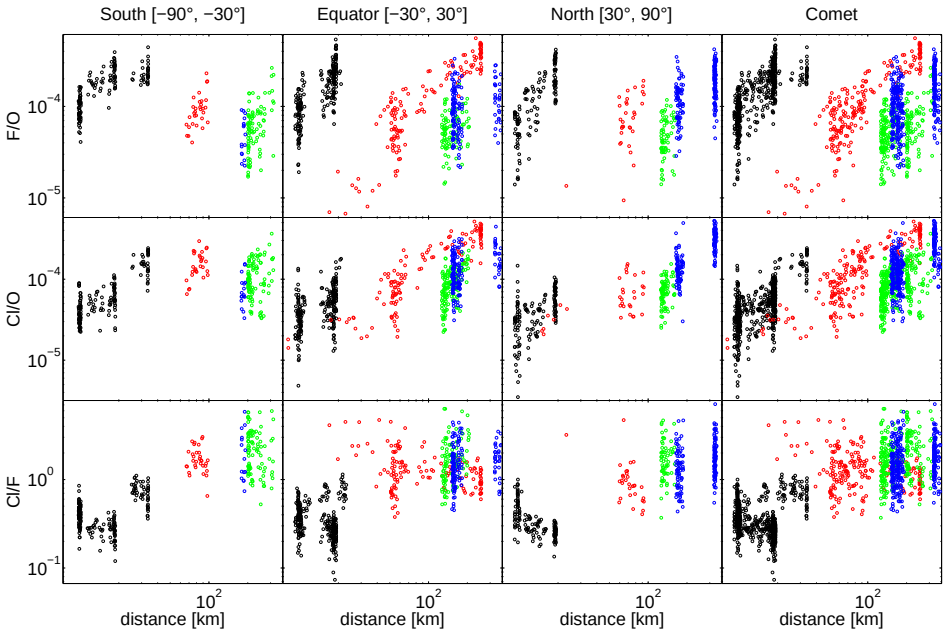

Figure 10. F/O, Cl/O, and Cl/F ratios as a function of cometocentric distance for southern, equatorial, northern and all latitudes (from left to right). Data from periods A, B, C, and D are given in black, red, green and blue, respectively. Note that the solar illumination (heliocentric distance and phase angle) and gas and dust production conditions are different for each period so that a mutual comparison is not trivial. Overall, Cl/O and Cl/F show an increasing trend with cometocentric distance.

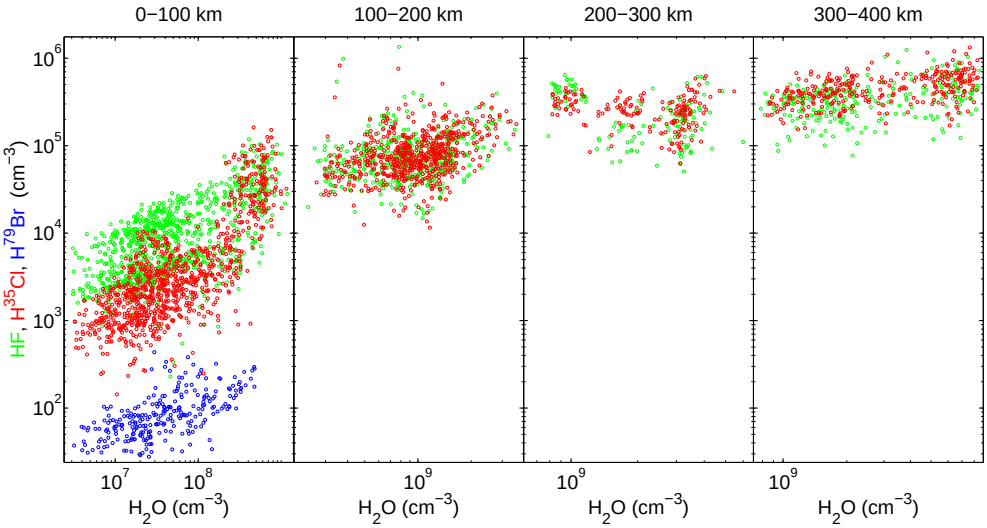

Figure 11. The correlation between HF, HCl, and HBr abundances and H_2O changes as a function of spacecraft distance from the comet (corresponding to an increase in comet activity).

tions are sensitive to systematic changes in overall comet activity and season during the time period considered (e.g. between the two periods covered by the analysis of event D). Results based only on scaled densities therefore cannot be considered conclusive.

A second argument for a distributed source interpretation for the halides is presented by Fig. 11. This figure sorts the data in four cometocentric distance bins; the bins cover all latitudes. For each of the bins, the correlation between the hydrogen halide abundances and H_2O is shown, mostly reflecting the diurnal variability. In all bins (except the sparsely populated 200–300 km bin) a clear correlation between both is found. Indeed, the hydrogen halide variations vary in sync with the water or total gas production during the diurnal cycle. The correlation coefficient, however, is always below unity, and decreases as one moves farther away from the nucleus, that is, the amplitude of the daily variation is weaker for the halogens than for H_2O and generally diminishes with distance. Since a larger distance of *Rosetta* from the comet corresponds to higher comet activity (a consequence of dust interfering with the star trackers) and, in fact, a higher grain-to-gas production ratio, this is

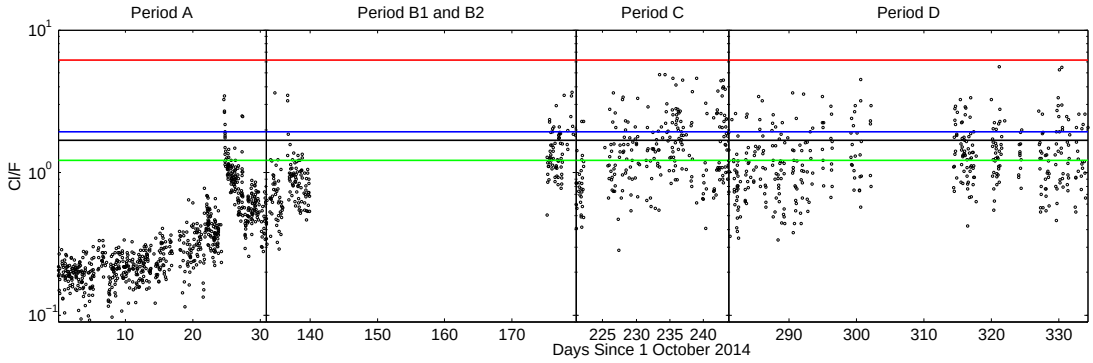

Figure 12. Cl/F ratio as a function of time for all observation periods. The black line represents the average for periods C and D, while the blue, red, and green lines indicate the ratios for Earth and for CI chondrites, and an upper limit for C/2009 P1 (Garradd), respectively (see Dhooghe et al. 2017, and references therein).

exactly what was found in Fig. 3 based on the distributed source model: when icy dust production is relatively more important, the halogen content becomes less dependent on the diurnal cycle. Indeed, gas sublimating from dust particles moving with a range of speeds well below the gas speed is distributed more uniformly and smoothes the daily variations with distance; this effect is more important when gas production from icy dust outweighs the gas production on the nucleus, so it matters for the hydrogen halides much more than for water. The same argument can help to explain why the observed hydrogen halide abundance asymmetry between northern and southern hemispheres is much less than the pronounced water or O element abundance asymmetry as observed around perihelion far from the nucleus (see Fig. 9).

When the distributed source gas is released within the collision-dominated inner coma, it will acquire the outward coma gas expansion speed (depending on the amount of gas deposited, it might actually slow down the coma gas). Wherever the gas is delivered to the coma in the non-collisional region, however, we hypothesize that the speed of a distributed source hydrogen halide molecule is small relative to the dust particle from which it originated. This is not unlikely when thermal desorption is the release process: as the particle progressively collects thermal energy, molecules at the surface might be desorbed as soon as they overcome the corresponding energy barrier. As long as this release speed is small relative to the particle speed, the gas supplied by the distributed source is still essentially moving radially outward and within the field of view of DFMS. If not, we might miss a fraction of the distributed source gas and therefore fail to obtain a correct assessment of the coma composition. This does not seem to be the case, however. Dhooghe et al. (2017) observe that the halogen-to-oxygen abundances established for 67P match the solar system abundances, so that no significant part of the halogen distribution appears to be missing. Therefore the observed smoothing of the spatial halogen-over-oxygen profiles must be mostly due to the range of speeds of the dust particles contributing to the distributed source. The changing slope seen in Fig. 11 can be interpreted as the daily density variation due to hydrogen halides sublimating from the nucleus surface being superposed on a relatively constant background that increases with distance from the nucleus. The speeds of the particles contributing to the distributed source may therefore cover a certain range, but should remain well below the gas speed, which is ~500 m/s; if not, the daily modulation would not be washed out so quickly.

A third argument for a distributed source interpretation are the observed variations in n_{Cl}/n_F. The n_{Cl}/n_F density ratio (Fig. 12) tends to fluctuate around 1.7 (average for periods C and D, reflecting the bulk composition, varying between 0.5 and 7.0), except in early October 2014. The variability in n_{Cl}/n_F near perihelion is found to be much more limited than in n_F/n_O and n_{Cl}/n_O, while this period was characterized by strong variations in gas and dust production. This can be easily understood in the context of a distributed source, as changes in dust production affect HF and HCl in a similar manner: while dust production changes, the composition of the grain mantles does not. The Cl/F profile can be interpreted as originating from two causes. First, the amount of chlorine released from the nucleus surface appears to be lower than that of fluorine, while the amount of chlorine in the dust particle mantles seems to be higher. Second, the fluorine and chlorine gradients in the refractory dust mantles may be different (see Section 2.1). The observed profile allows for an assessment of the extent of the distributed source: the bulk Cl/F composition is typically reached beyond 30 km (the cometocentric distance of *Rosetta* on day 50 of period A is 30 km, while it is 40–60 km early in period B1; note that the size of the source is expected to change upon approaching the Sun).

In early October 2014, when *Rosetta* was close to the comet, the comet was still outside the water snowline and dust activity was limited. The low n_{Cl}/n_F observed at that time reflects the composition of material sublimating and/or sputtered (Wurz et al. 2015) from the nucleus surface. By the end of October 2014, n_{Cl}/n_F intermittently reaches the bulk value with an abrupt enhancement by a factor of about 5 around noon on 24 October, slowly falling back over a few days, and with recurring enhancements over 3 rotation periods. This enhancement is due to higher number densities for Cl, while F and O follow the diurnal cycle. It is difficult to assign such rapid and dramatic changes to compositional variations over the surface or to a time-dependent localized volatile source on the nucleus: since DFMS at any

time accepts neutrals from all over the visible surface, such an interpretation would require an unrealistically intense Cl-enriched local source. However, the observed variability is compatible with, for instance, a localized change of the dust particle size spectrum. If smaller particles become prevalent (possibly after surface events such as cliff collapse or pit formation that involve extensive pre-fracturing of the material and that have shown to imply a steepening of the size spectrum on the metre scale (Pajola et al. 2015, 2017)), mantle sublimation happens faster, which affects the total chlorine content much more than the fluorine content (since the neutral gas from the nucleus is richer in fluorine).

4 CONCLUSIONS

We have presented different lines of evidence from *Rosetta*/ROSINA-DFMS observations of the hydrogen halides that indicate that aggregates of refractory dust particles covered with a halogen-enriched icy mantle constitute a distributed source of HF and HCl in the inner coma of comet 67P/Churyumov-Gerasimenko:

- When disentangling all sources of variability in the coma gas, the HF and HCl abundances relative to the total neutral gas content are found to increase with distance from the nucleus, which can only be ascribed to a distributed source since no other halogen-bearing parent with sufficient abundance has been found.
- The amplitude of the daily variability in the hydrogen halide densities decreases significantly with cometocentric distance. Similarly, at large distance there is much less hemispheric asymmetry for the hydrogen halides than for water. These characteristics can only be explained by a distributed source from dust particles with a certain dispersion in their outward speeds.
- The variability of the Cl/F ratio as observed by DFMS, and the lack thereof at large distance, can only be understood in terms of a dust-related source containing hydrogen fluoride and hydrogen chloride, with more fluorine sublimating from the comet, and a higher proportion of chlorine in the dust particle mantle material. The Cl/F ratio indicates a distributed source extending out to about 30 km.
- From the above it can be inferred that icy aggregates with a size on the order of 100 μm or larger and with speeds well below the gas speed are likely delivering most of the hydrogen halides to the coma. Such aggregates constitute a minor fraction of the total mass production, so that the contribution to a distributed water source remains small and so that dust fragmentation occurs for not more than a few percent of all dust particles.

Knowing that the halogens freeze out onto refractory dust particles in molecular clouds as soon as water ice starts forming on the particle surface (Kama et al. 2015), the icy mantles of such particles should be layered, with a halogen density enrichment near the surface. Halogen delivery to the coma must be accompanied by delivery of water (and other species trapped in the mantle ice), but for water the relative contribution is expected to be minor.

In a certain sense this distributed source has already been seen indirectly by Agarwal et al. (2016), who report the observation of the acceleration of decimetre-size aggregates in the lower coma with the OSIRIS cameras: This acceleration is ascribed to the rocket force from asymmetric outgassing, which almost inevitably must involve sublimation of the majority ice component H_2O to provide sufficient thrust. Also Gicquel et al. (2016) infer sublimation of icy aggregates in the coma from the brightness profiles of dust jets. Using a sophisticated model of grain sublimation, they find that typical dirty water-ice grain sizes in jets are in the range 10–100 μm and that most of these grains sublimate on a length scale on the order of or larger than 10 km (but their observations were limited to 10 km cometocentric distance). The fact that the amplitude of the daily variability in the oxygen element densities does not significantly decrease with cometocentric distance proves that the relative contribution from a distributed source of water is small, in agreement with the findings of Fulle et al. (2016a). The limited extent of the distributed source inferred here is by no means in conflict with the earlier established fact that there is no evidence of fragmentation or sublimation from 100 km up to the outer coma (Fulle et al. 2016c).

A practical consequence of the existence of distributed sources is that it may be difficult to properly assess the average fraction of minor volatiles in the composition of the nucleus. On the one hand, not all of the dust mantle material may have sublimated yet in the inner coma, so that abundance measurements there might lead to an underestimation of the material's abundance. On the other hand, farther away from the nucleus various loss processes (photodissociation, photo-ionization, charge exchange, and other reactions) might become important. The only option is to use coma chemistry models to try to match the observations of minor species abundances.

The very existence of a distributed source for the halogen halides confirms that they are stored in the icy mantles of dust particles, and offers yet another argument in favor of the hypothesis put forward by Dhooghe et al. (2017) that all halogens were locked up in the form of hydrogen halides on grains in the protosolar cloud and were incorporated in the comet during planetesimal aggregation.

ACKNOWLEDGEMENTS

The authors would like to thank the following institutions and agencies, which supported this work: Work at BIRA-IASB was supported by the Belgian Science Policy Office via PRODEX/ROSINA PEA90020 and 4000107705 and by the F.R.S.-FNRS grant PDR T.1073.14 "Comparative study of atmospheric erosion". AG acknowledges an Additional Researchers Grant (Ministerial Decree of 19/12/2014), as well as a FRIA grant from the F.R.S.-FNRS. Work at UoB was funded by the State of Bern, the Swiss National Science Foundation, and by the European Space Agency PRODEX Program. Work at MPS was funded by the Max-Planck Society and BMWI under contract 50QP1302. Work at Southwest Research Institute was supported by subcontract #1496541 from the Jet Propulsion Laboratory. This work was supported by CNES grants at IRAP, LATMOS, LPC2E, CRPG, and by the European Research Council (grant no. 267255 to B. Marty). Work at the University of Michigan was funded by NASA under contract JPL-1266313. ROSINA would not give such outstanding results without the work of

the many engineers, technicians, and scientists involved in the mission, in the *Rosetta* spacecraft, and in the ROSINA instrument team over the last 20 years whose contributions are gratefully acknowledged. *Rosetta* is an ESA mission with contributions from its member states and NASA. We acknowledge herewith the work of the whole ESA *Rosetta* team. All ROSINA data have been / will be released to the PSA archive of ESA and to the PDS archive of NASA.

REFERENCES

Agarwal J., et al., 2016, MNRAS, 462, S78
Altobelli N., et al., 2016, Science, 352, 312
Ayotte P., Rafiei Z., Porzio F., Marchand P., 2009, J. Chem. Phys., 131, 124517
Ayotte P., Marchand P., Daschbach J. L., Smith R. S., Kay B. D., 2011, J. Phys. Chem. A, 115, 6002
Balsiger H., et al., 2007, Space Sci. Rev., 128, 745
Balsiger H., et al., 2015, Sci. Adv., 1, e1500377
Bartels-Rausch T., et al., 2014, Atmos. Chem. Phys., 14, 1587–
Bentley M. S., et al., 2016, Nature, 537, 73
Bieler A., et al., 2015a, Nature, 526, 678
Bieler A., et al., 2015b, A&A, 583, A7
Calatayud M., Courmier D., Mino C., 2003, Chem. Phys. Lett., 369, 287–
Cervinka C., Fulem M., 2017, J. Chem. Theory Comput.
Collings M. P., McCoustra M. R. S., 2005, Proc. IAU, 1, 405–414
Collings M., Anderson M., Chen R., Dever J., Viti S., Williams D., McCoustra M., 2004, MNRAS, 354, 1133
Cottin H., Fray N., 2008, Space Sci. Rev., 138, 179
Della Corte V., et al., 2014, J. Astron. Instr., p. 1350011
Delzeit L., Rowland B., Devlin J. P., 1993, J. Phys. Chem., 97, 10312
Dhooghe F., et al., 2017, MNRAS, this issue
Emprechtinger M., Monje R. R., van der Tak F. F. S., van der Wiel M. H. D., Lis D. C., Neufeld D., Phillips T. G., Ceccarelli C., 2012, Astrophys. J., 756, 136
Fayolle E. C., Öberg K. I., Cuppen H. M., Visser R., Linnartz H., 2011, A&A, 529, A74
Fayolle E. C., et al., 2017, Nature Astronomy, 1, 703
Feistel R., Wagner W., 2007, Geochim. Cosmochim. Acta, 71, 36
Fink U., et al., 2016, Icarus, 277, 78
Fougere N., et al., 2016, A&A, 588, A134
Fulle M., Altobelli N., Buratti B., Choukroun M., Fulchignoni M., Grün E., Taylor M. G. G. T., Weissman P., 2016a, MNRAS, 462, S2
Fulle M., et al., 2016b, MNRAS, 462, S132
Fulle M., et al., 2016c, ApJ, 821, 19
Fulle M., et al., 2017, MNRAS, 469, S45
Fuselier S. A., et al., 2015, A&A, 2, 1
Gasc S., et al., 2017, MNRAS, 469, S108
Gicquel A., et al., 2016, MNRAS, 462, S57–S66
Hadamcik E., Levasseur-Regourd A. C., Hines D. C., Sen A. K., Lasue J., Renard J.-B., 2016, MNRAS, 462, S507
Hansen K. C., et al., 2016, MNRAS, 462, S491
Hässig M., et al., 2015, Science, 347, aaa0276
Hilchenbach M., et al., 2017, Phil. Trans. Royal Soc. A, 375
Huebner W. F., Mukherjee J., 2015, Planet. Space Sci., 106, 11
Inaba A., Chihara H., 1978, J. Chem. Thermodyn., 10, 65
Kama M., et al., 2015, A&A, 574, A107
Keller H. U., et al., 2007, Space Sci. Rev., 128, 433
Kissel J., et al., 2007, Space Sci. Rev., 128, 823
Le Roy L., et al., 2015, A&A, 583, A1
Lien D. J., 1990, Astrophys. J., 355, 680
Luna R., Satorre M. Á., Santonja C., Domingo M., 2014, A&A, 566, A27
Luspay-Kuti A., et al., 2015, A&A, 583, A4
Mannel T., Bentley M. S., Schmied R., Jeszenszky H., Levasseur-Regourd A. C., Romstedt J., Torkar K., 2016, MNRAS, 462, S304–S311
Nilsson H., et al., 2015, Science, 347, aaa0571
Nilsson H., et al., 2017, MNRAS, this issue
Olanrewaju B. O., Herring-Captain J., Grieves G. A., Aleksandrov A., Orlando T. M., 2011, J. Phys. Chem. A, 115, 5936
Opitom C., Jehin E., Manfroid J., Hutsemékers D., Gillon M., Magain P., 2015, A&A, 574, A38
Pajola M., et al., 2015, A&A, 583, A37
Pajola M., et al., 2017, Nature Astronomy, 1, 0092
Parent P., Laffon C., 2005, J. Phys. Chem. B, 109, 1547
Park S.-C., Kang H., 2005, J. Phys. Chem. B, 109, 5124
Pätzold M., et al., 2016, Nature, 530, 63
Peng R., Yoshida H., Chamberlin R. A., Phillips T. G., Lis D. C., Gerin M., 2010, Astrophys. J., 723, 218
Riedler W., et al., 2007, Space Sci. Rev., 128, 869
Rotundi A., et al., 2015, Science, 347, aaa3905
Rubin M., Tenishev V. M., Combi M. R., Hansen K. C., Gombosi T. I., Altwegg K., Balsiger H., 2011, Icarus, 213, 655
Rubin M., et al., 2015, Science, 348, 232
Schläppi B., et al., 2010, J. Geophys. Res., 115, A12313
Schulz R., et al., 2015, Nature, 518, 216
Ser F., Larher Y., 1990, J. Chem. Thermodyn., 22, 407
Svanberg M., Pettersson J. B. C., Bolton K., 2000, J. Phys. Chem. A, 104, 5787
Toubin C., Picaud S., Hoang P. N. M., Girardet C., Lynden-Bell R. M., Hynes J. T., 2003, J. Chem. Phys., 118, 9814
Vinodkumar M., Dave R., Bhutadia H., Antony B. K., 2010, Int. J. Mass Spectrom., 292, 7
Viti S., Collings M. P., Dever J. W., McCoustra M. R. S., Williams D. A., 2004, MNRAS, 354, 1141
Westphal A. J., et al., 2014, Science, 345, 786
Wolff E. W., Mulvaney R., Oates K., 1989, Geophys. Res. Lett., 16, 487
Wurz P., et al., 2015, A&A, 583